Multi-scale analysis of the diffusion barrier layer of gadolinia-doped ceria in a Solid Oxide Fuel Cell operated in a stack for 3000 h

M. Morales (1), V. Miguel-Pérez (1), A. Tarancón (1), A. Slodczyk (1), M. Torrell (1), B. Ballesteros (2), J. P. Ouweltjes (3), J. M. Bassat (4), D. Montinaro (5), A. Morata (1)*

(1) IREC, Catalonia Institute for Energy Research, Dept of Advanced Materials for Energy Applications, Jardins de les Dones de Negre 1, Planta 2, 08930, Sant Adriá del Besós, Barcelona, Spain.

(2)) Catalan Institute of Nanoscience and Nanotechnology (ICN2), CSIC and The Barcelona Institute of Science and Technology, Campus UAB, Bellaterra, 08193 Barcelona, Spain.

(3) HTceramix SA, Avenue des Sports 26, CH-1400 Yverdon-les-Bains, Switzerland

(4) CNRS, ICMCB, 87 avenue du Dr. A. Schweitzer, F-33608 Pessac, France.

(5) SOLIDPower SpA, Viale Trento 117, 38017 Mezzolombardo, Italy.

Corresponding author: amorata@irec.cat

Abstract

The state-of-the-art materials for SOFCs are yttria-stabilized zirconia as electrolyte and lanthanum strontium cobalt ferrite as cathode. However, the formation of insulating phases between them requires the use of diffusion barriers, typically made of gadolinia doped ceria. The study of the stability of this layer during the fabrication and *in operando* is currently one of the major goals of the SOFC industry. In this work, the cation inter-diffusion at the cathode/barrier layer/electrolyte region is analyzed for an anode-supported cell industrially fabricated by conventional techniques, assembled in a short-stack and tested under real operation conditions for 3000h. A comprehensive study of this cell, and an equivalent non-operated one, is performed in order to understand the inter-diffusion mechanisms with possible effects on the final performance. The analyses evidence that the cation diffusion is occurring during the fabrication process. Despite the significant diffusion of Ce,Gd, Zr, Y and Sr cations, the formation of typically reported CGO-YSZ solid solution is not observed while the presence of isolated grains of $SrZrO_3$ is proved. All in all, this study presents new insights into the stability of the typically employed diffusion barriers for solid oxide cells that will guide future strategies to improve their performance and durability.

Keywords: Strontium, Zirconium, Cation diffusion, $SrZrO_3$, CGO interlayer, SOFC, Raman spectroscopy

1. Introduction

Solid oxide fuel cells (SOFCs) are efficient energy conversion devices that directly transform chemical energy of fuel into electricity **[1]**. The future of SOFCs depends on the development of efficient and robust materials capable to withstand long times at high temperature and typical harsh ambient conditions during operation. Current developments in SOFCs are focused on increasing the power density and minimizing degradation during operation. A number of factors, such as operation conditions, materials, design and environment promote different types of degradation processes that can have a significant influence on the cell performance **[2,3]**. A typical phenomenon related to the low performance and degradation of SOFCs is the reduction of the power output due to element diffusion and phase segregation in its different components. These processes can also substantially change the material composition near the interfaces, leading to low performing regions. Inter-diffusion may occur during heat treatments for co-sintering of cell layers, but also during long term cell operation.

One of the main contributions to the poor performance and degradation comes from the cathode electrode. Several authors have evaluated the importance of cation diffusivities for surface segregation of Sr and thus for a major degradation mechanism of SOFC cathodes **[4,5]**. Currently, mixed ionic–electronic conductors (MIECs), such as lanthanum strontium cobalt iron oxide $La_{1-x}Sr_xCo_{1-y}Fe_yO_3$ (LSCF), are used as cathode due to their high catalytic activity, as well as good ionic and electronic conductivities at intermediate temperatures **[6]**. The reaction of LSCF with the YSZ electrolyte at high temperatures forming insulating secondary phases is a well-known phenomenon **[7,8,9]**. Strontium zirconate ($SrZrO_3$) and lanthanum zirconate ($La_2Zr_2O_7$) are generated, thus potentially forming ion blocking layers in critical regions such as the cathode-electrolyte interface. A side effect of this element diffusion is the formation of inert phases with low electrical conductivity like Co_3O_4 at regions where Sr can be expelled from the LSCF structure **[10,11,12]**. A standard solution to avoid the crystallization of these phases is the introduction of a Gd or Sm-doped CeO_2 (CGO, SDC, respectively) layer between the cathode and the electrolyte, which acts as a barrier layer for the Sr diffusion **[9,13,14]**.

The inter-diffusion barrier layers fabricated by conventional deposition techniques, like screen-printing or spraying-coating, generally present a wide thickness range of 4 to 10 μm **[15]**. Few exceptions, like the work of Van Berkel et al. **[16]** present thinner screen-printed ceria barrier layers (1.4 μm, in this case). The porosity of these deposited and sequentially sintered CGO layers may be in the range 20-30%, even after sintering at 1300ºC **[17,18]**. In addition, the ionic conductivities of the CGO barrier layers are lower than the expected. This has been attributed to different factors, like an inter-diffusion between CGO and YSZ, leading to CGO_x:$YSZ_{(1-x)}$ solid

solutions with high ionic resistances **[19,20,21],** the formation of resistive phases involving cathode species **[9]**, and the appearance of the so-called Kirkendall voids, produced by the Ce diffusion into the YSZ **[22]**.

Understanding the formation of the barrier layer region and its evolution along the operating lifetime is challenging due to the high complexity of the system and the number of processes that simultaneously take place and eventually interact. In the present work, a comprehensive multi-scale characterization of the CGO barrier layer and its interfaces has been carried out, combining different complementary analysis techniques at micro- and nano-scale levels. Representative samples have been used, comparing a non-operated cell with another coming from a cell operated in a stack under real conditions for 3000 h. The morphologic study carried out by Scanning Electron Microscopy (SEM) and Transmission Electron Microscopy (TEM) is completed with the observation of element distribution maps obtained by Energy Dispersive X-Ray Spectroscopy (EDX), Electron Probe Micro Analysis with Wavelength Dispersive X-Ray (EPMA-WDX), Secondary Ion Mass Spectroscopy (SIMS) and Electron Energy Loss Spectroscopy (EELS). Finally, micro-Raman Spectroscopy has provided complementary information about the presence of specific phases at a local level **[23,24,25,26]**.

The final aim of this work is to give a broad multi-scale experimental basis that allows understanding the inter-diffusion phenomena taking place in the SOFC barrier layer.

2. Experimental procedure

The degradation studies were performed on an anode supported cell from a stack with planar configuration. The SOFC stack consisted of coated ferritic stainless steel interconnectors, cells and glass seals. The cells were supported on a nickel- yttria-stabilized zirconia (Ni-YSZ) cermet anode with YSZ as electrolyte and a lanthanum strontium cobalt ferrite oxide (LSCF) as a cathode material. $Ce_{0.9}Gd_{0.1}O_{1.95}$ (CGO) was used as a barrier layer between cathode and electrolyte to prevent the formation of poorly conducting secondary phases, such as $SrZrO_3$ or $La_2Zr_2O_7$. The cells were tested for 3000 h at 780 ºC in a short-stack in order to characterize the cells under real conditions, using dry H_2 as fuel in the anodic compartment and air in the cathodic chamber.

The cross-sectional cell analysis of the diffusion of the cations across the cathode-interlayer-electrolyte was performed by Confocal Laser Raman Spectroscopy and Scanning Electron Microscope equipped with Electron Probe Micro Analysis with Wavelength Dispersive X-Ray

(EPMA-WDX). In this analysis, the composition of the oxide scale was identified using the Powder Diffraction File (PDF) database **[27]**.

SIMS experiments were carried out using a Time of Flight Secondary Ion Mass Spectroscopy (TOF-SIMS) device from Ion ToF company (Tof SIMS5). This technique uses a pulsed ion beam (here Bi+) to remove both atoms and molecules from the sample surface (< 4 monolayers). The secondary ions removed from the surface are then extracted and accelerated by an electrical field and their masses are then determinate by measuring their time of flight over the analyzer to reach the detector.

The reference Raman spectra were recorded using a Horiba Spectrometer HR800 (LabRAM Series, Horiba Jobin Yvon). The 532 nm excitation line and 100x objective were applied. In order to assess the possible formation of $(Zr,Ce)O_2$-based solid solutions and the formation of secondary insulating phases 2D XY Raman mappings were performed on the cross section of the LSCF/CGO/YSZ interfaces. The mapping was recorded using the DXR xi Raman microspectrometer (Thermo Fisher). This spectrometer enables the high resolution (0.5 µm) mapping recorded on a large cross section area (21 lines were recorded, each composed of 87 pixel, leading to images formed by 1827 Raman spectra). Similarly, 532 nm wavelength and 100x objective were used.

The microstructure of samples was examined by Scanning Electron Microscopy (SEM, Zeiss Auriga) equipped with an Oxford Inca Pentafet X3 Energy Dispersive X-ray Analyser. Due to an overlap of the emission lines for the Lα-series in the characteristic X-ray spectra of strontium and zirconium, the elemental analysis and phase distribution in the cross section were studied using a JEOL JXA-8230 Scanning Electron Microscope (SEM) equipped with an Electron Probe Micro Analyser with Wavelength Dispersive Spectrometer (EPMA-WDX). The spatial distributions of Ce, La, Sr, Zr and elements were determined by EPMA-WDX mapping over LSCF/CGO/YSZ interfaces in order to evaluate their chemical reaction behaviour in fresh and aged cells.

The study of local microstructural and phase distribution was carried out by Transmission Electron Microscopy (TEM), and a High Resolution Scanning Electron Microscopy (HRSEM) coupled with an Oxford Inca Pentafet X3 EDX. Moreover, the samples were characterized by EDX and Electron Energy Loss Spectroscopy (EELS) used in Scanning Transmission Electron Microscopy (STEM) mode to investigate variations in cation concentrations at the grain boundaries. For TEM observations, a lamella was prepared by the Focused Ion Beam (FIB) on a Zeiss using a gallium source. Before cutting, a Pt line was usually deposited on the area of interest to protect the top portion of the specimen and to mark the position of the target area. The lamella was thinned to a

thickness of approximately 100 nm. Also, cross-sectional TEM samples were prepared by standard manual grinding and thinning procedures. A final polishing step was conducted in a Precision Ion Polishing System (PIPS 691, Gatan). High Resolution Transmission Electron Microscopy (HRTEM) was employed to obtain information about the internal structure. HRTEM and STEM-EDX maps were acquired at 200 kV on a JEOL JEM 2100 equipped with an Oxford Instruments INCA system for collecting EDX spectra. High angle annular dark field (HAADF) STEM images, STEM-EDX and STEM-EELS elemental profiles were obtained at 200 kV using a FEI Tecnai G2 F20 coupled with a GIF Quantum energy filter and a an EDAX super ultra-thin window (SUTW) X-ray detector. It is important to note that for the Gd EELS profiles the Gd-M_4 edge (at 1217 eV) was used. The Gd-M_5 edge (at 1185 eV), although more intense, overlaps with the Ce-M_3 edge (also at 1185 eV) and therefore is not suitable for the Gd determination.

3. Results and discussion

3.1 Microstructural analysis in the vicinity of the CGO barrier layer region

The microstructure of the different layers surrounding the electrolyte is presented in **Figure 1a**, which provides a representative cross section image of the fresh cell morphology. The LSCF-CGO and Ni-YSZ composites constituting the cathode and anode, respectively, present a porous homogeneous microstructure. The YSZ electrolyte is dense, only showing closed porosity. The thickness of this component is approximately 8 µm. A homogeneous CGO layer separating the cathode from the electrolyte is easily distinguishable, presenting a thickness of around 3 µm. The expanded image (**Figure 1b**) reveals a significant porosity and relatively large grains. The attachment between the barrier layer and the electrolyte is excellent. Relevant differences between the fresh and aged samples have not been observed in the microstructure of any of the explored layers and interfaces.

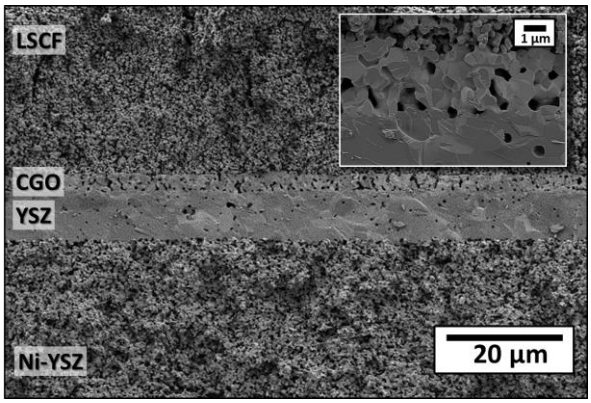

Figure 1. Cross-sectional SEM micrographs of a fresh cell. The inset corresponds to a higher magnification of the barrier layer region.

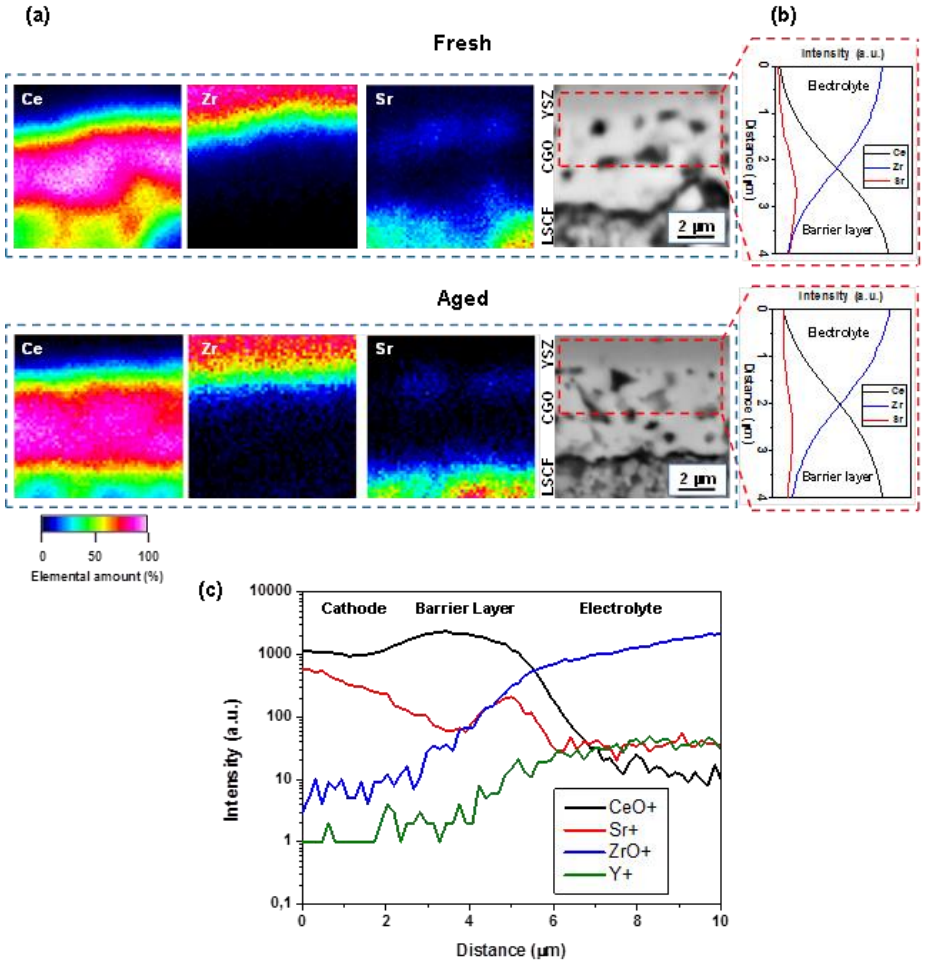

Figure 2. **(a)** Cross sectional BSE images and EPMA elemental distribution maps of Ce, Zr and Sr. **(b)** WDX elemental cross section profiles across CGO/YSZ interface (red rectangular discontinuous area) in fresh and aged cells. **(c)** SIMS depth profiles of LSCF/CGO/YSZ, after the sintering process of the cathode for the aged cell.

3.2 Cation diffusion from cathode and electrolyte through the CGO barrier layer

This section will be focused on assessing the efficiency of the CGO layer as a diffusion barrier for hindering the interaction between the cathode and electrolyte cations, and preventing the formation of insulating phases. First, EPMA-WDX mappings on the cross sections of fresh and aged cells (**Figure 2a**) revealed that Sr is diffusing through the barrier layer in both cases, presenting accumulation clusters in zones close to the electrolyte. Mappings were also obtained from all the other elements present in the cathode (not shown here), without revealing any further sign of diffusion. In addition, cross-sectional element profiles were determined by extracting selected areas from the CGO/YSZ interface (**Figure 2b**). The elemental distribution indicated that the diffusion of Zr and Ce, between the electrolyte and the barrier layer, and Sr from the cathode to the electrolyte took place in both samples. An accumulation of Sr at the interface between the

electrolyte and the CGO layer is evidenced. Remarkably, no significant differences appeared between aged and fresh samples. This suggests that the element diffusion was mainly produced during the different sintering processes, not during operation. Therefore, it can be concluded that the inter-diffusion of the species from the barrier layer and the electrolyte takes place during the CGO sintering process. The annealing of the cathode is accompanied by a diffusion of Sr through the barrier layer to the electrolyte. For this reason, in order to simplify the explanations, subsequent results of different analytical techniques will be presented indistinctly for aged or fresh cells. The focus will be put on the diffusion of: i) the species from the YSZ and the CGO that occurs during the processing of the barrier layer, and ii) the Sr diffusion happening during the cathode co-sintering.

3.2.1 Ce and Zr diffusion

The diffusion of Ce and Gd, from the barrier layer, and Zr and Y, from the electrolyte, taking place during the sintering of the CGO has an important impact on the barrier layer performance **[28]**. It has been widely reported that, exceeding a certain temperature of sintering, an increased electrical resistance of the barrier layer produces an important reduction of the cell performance **[19-21,29,30]**. This is an impediment for achieving the optimum densification required for improving the blocking of cathode ions diffusion to the electrolyte. Here, several complementary techniques have been added to the elemental distribution shown in the previous section in order to study the phenomena associated to the Zr, Y, Ce and Gd diffusion at the CGO/YSZ interface. Raman spectroscopy has been used for gaining insights into the crystal structure of species resulting from the cation inter-diffusion. STEM-EDX and EELS have been employed in order to locally determine the specific position of cations in this region.

Figure 2c exhibits the elemental distribution of the LSCF/CGO/YSZ region analysed by depth-profiling SIMS in the case of the aged cell, showing the concentration of elements at different depths. Although quantitative determination of the relative concentration of species is not possible, this technique provides information about the evolution of the amount of elements along the studied layers. For example, similarly to elemental mappings presented above (**Figure 2a-b**), an overlapping between Zr and Ce close to the electrolyte/barrier layer interface is clearly evidenced, indicating a significant diffusion along distances of several microns. The comprehension of the CGO and YSZ inter-diffusion is crucial since it can lead to the formation of the CGO-YSZ solid solutions at high sintering temperatures. According to previous studies, such solution, presenting lower ionic conductivity, can be formed by the Ce component diffusion into YSZ across the CGO/YSZ interface, leading to Kirkendall pores in the CGO **[29,31]**. It should be stressed however that this easy formation of solid solution is mostly detected in the case of powders co-sintered together **[32]**. In the case of dense ceramic material, the presence of the solid solution is not systematically observed **[33]** showing that complementary analyses sensitive to the Zr, Ce and Gd

presence and their chemical interaction are necessary in order to determine both the possible presence of CGO-YSZ solid solutions at CGO/YSZ interface and the Gd diffusion. It is important to mention here that, to the best of our knowledge, the existence of Gd diffusion has not received much attention in the literature, but at specific studies from Uhlenbruck et al. **[9]** and Wang et al. **[10]**.

Figure 3 shows the results obtained from a 2D Raman mapping performed on the cross section of the sample in a region comprising the CGO layer and part of the YSZ electrolyte. The spatial resolution of the experiment was determined by the laser spot size, which is around 400 nm. The highly intense peak presented by CGO at around 460 cm^{-1} (F_{2g} mode) allowed a fast acquisition, i.e. the study ofrepresentative areas. On the other hand, YSZ showed a very characteristic Raman fingerprint near 610 cm^{-1} clearly distinguishable in the spectra acquired at the electrolyte region **[34].** The surface plot in **Figure 3a** represents the intensity of the main CGO peak. The direction perpendicular to the layers is represented by the x axis, choosing the CGO-YSZ interface as the origin. The CGO layer is then located in the positive side while increasing negative x values correspond to points deeper inside the electrolyte. In the insets, some spectra from three positions (-3, 0 and 3.5 µm) have been extracted in order to illustrate the nature of the outcomes along the cross section. Although the intensity of the peak does not allow direct quantification of the proportion of CGO present in the spot area, it can be assumed that larger peak intensity implies higher concentration. Thanks to the high sensitivity of Raman to cerium oxide-based phases, the deep diffusion of Ce into the electrolyte is clearly evidenced. Ce-based oxides are detected even 3 microns away from the CGO barrier layer, which is consistent with the STEM-EDX elemental distribution maps of Ce and Zr at the CGO/YSZ shown in **Figures 4a-c** and was also indicated by SIMS (**Figure 2d**). This Ce and Zr diffusion at the CGO/YSZ interface is expected to occur during the sintering process and has been previously reported **[21]**.

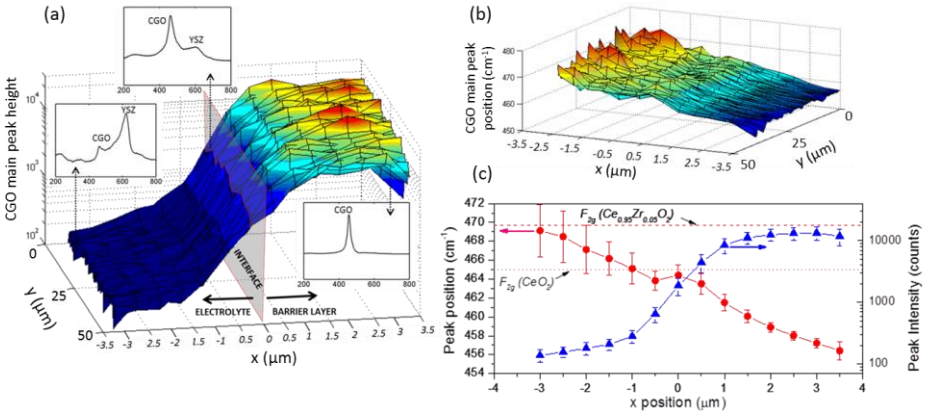

Figure 3. **(a)** Intensity of the F_{2g} Raman peak of the CGO at different points of the surface and depth. The electrolyte-barrier layer interface has been taken as origin of coordinates (positive direction corresponding to barrier layer, negative going deep in the electrolyte). The insets show examples of the spectra acquired at different x positions. **(b)** Evolution of the F_{2g} peak of CGO along the surface, taking the same criteria for the coordinates as in (a). **(c)** Average values of peak position and intensity as a function of x position.

Further information is provided by Raman about the crystalline nature of the ceria-based compounds along the sample. All the recorded spectra are consistent with doped ceria, while, interestingly, the presence of the $(Zr,Ce)O_2$-based solid solution is not observed along the barrier layer. It is important to remark that most of the authors point such CGO-YSZ solid solution phase as the main mechanism leading to high resistances at elevated sintering temperatures and, therefore, as the limitation for the barrier layer densification **[21]**. Instead, the here presented results indicate a coexistence of both phases, i.e. YSZ and CGO, in a composite-like behaviour **[33]**. This can be evidenced by a careful analysis of the position, width and intensity of both characteristic CGO and YSZ Raman modes **[35]**.As shown in **Figure 3b,** the CGO peak shifts from 455 cm^{-1} at the interface with the cathode, that corresponds to a highly Gd-doped ceria **[36],** to 464 cm^{-1} in the CGO-YSZ interface. In addition, a peak shift is detected inside the electrolyte, reaching a maximum value of 470 cm^{-1} in the region when Ce-oxide is limited to traces (very low intensity peak) and when locally, from the Raman point of view, the YSZ cubic symmetry evolves into the tetragonal one. Continuous increase of CGO position at the barrier layer is an unambiguous phenomenon that can be attributed to the loss of Gd from CGO **[37].** Note that, in the CGO-YSZ interface, almost pure CeO_2 is present. Taking into account that pure CeO_2 presents an ionic conductivity around two orders of magnitude lower than an optimally doped ceria, a loss of dopant from the barrier could derive in a drastic increase of the resistance of the layer **[37,38]**.

In order to reinforce this hypothesis, STEM-EELS analysis was carried out looking for heterogeneities on the Gd concentration at the barrier layer. **Figures 4d-e-f** clearly show a segregation of Gd at the CGO grain boundaries from the barrier layer. This could indicate that CGO grain boundaries are fast diffusion paths for Gd, which can be the source of a gradual doping loss at the barrier layer when approaching the electrolyte. Further investigations are currently ongoing in order to determine the real impact that Gd loss and segregation has on the cell performance.

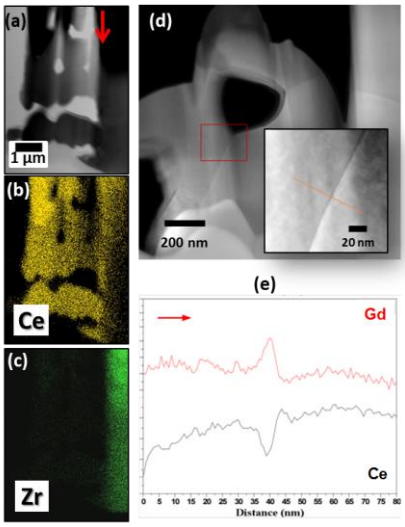

Figure 4. (a) Cross-sectional TEM micrograph of CGO/YSZ interface for the aged cell, **(b)** and **(c)** STEM-EDX elemental distribution maps of Ce and Zr. The red arrow in (a) indicates the approximate position of the barrier layer/electrolyte interface. **(d)** HAADF-STEM images of CGO grain boundary near CGO/YSZ interface. The inset corresponds to a higher magnification image indicating the region of the mapping in (e). **(e)** STEM-EELS Ce and Gd profiles across the CGO grain boundary.

3.2.2 Sr diffusion

With the aim of precisely determining the spatial distribution and generated phases at the regions where the Sr is present at the CGO/YSZ interface, compositional and microstructural analyses were carried out by SIMS, STEM-EDX and TEM. SIMS analysis clearly exhibits the accumulation of Sr close to the CGO/YSZ interface (**Figure 2c**), as it was previously observed by means of EPMA-WDX (**Figure 2a,b**). However, in this case, it is possible to observe the gradual decrease of the Sr concentration from the cathode through the CGO, being present in relatively large amounts along the whole barrier layer. In **Figure 5**, the STEM-EDX element distribution map of the CGO/YSZ interface also shows an enrichment of Sr near the electrolyte. Noteworthy, Sr was mainly observed close to the pores (i.e. regions 1 and 3), being absent in bulk (i.e., area 2). This arrangement of the Sr accumulation can suppose an attenuation of the effect of the isolating phases as, although constricting the effective oxide anion conduction area, it still provides free non blocked pathways where CGO and YSZ are in close contact. The accumulation of Sr in the pores of the CGO layer can indicate that diffusion took place mainly through the CGO grain surfaces **[39]**. In the next section, specific analysis will be presented with the aim of determining the role of CGO surfaces, such as free surfaces (close and open pores) and grain boundaries, in the Sr diffusion.

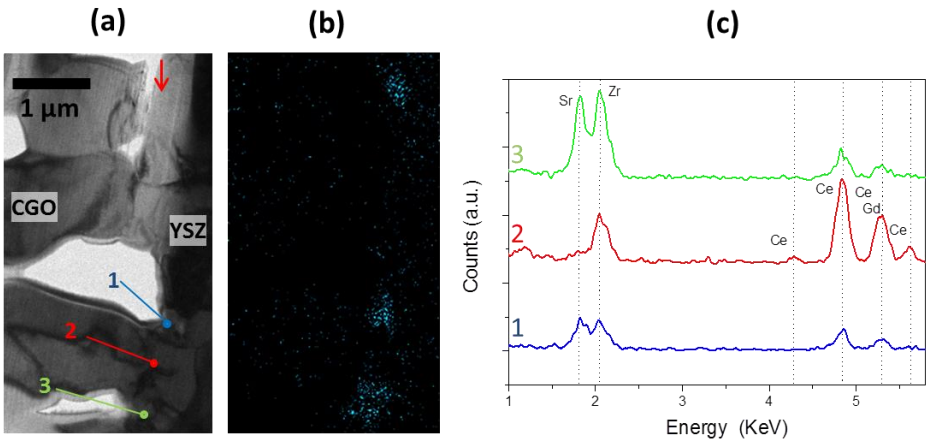

Figure 5. (a) TEM micrograph of the CGO/YSZ interface of an aged sample. The red arrow indicates the approximate limit of the barrier layer/electrolyte interface. **(b)** STEM-EDX elemental distribution maps of Sr, and **(c)** three different areas analysed by EDX.

TEM observations were also carried out in different regions inside the CGO barrier layer, in order to determine the formation of phases associated to the Sr diffusion evidenced in the SIMS profile and STEM-EDX maps. **Figure 6a** shows a TEM micrograph of the CGO barrier layer, in which two different areas (1 and 2) were analysed by EDX. Results indicate that area 1 is a segregate composed of Sr and Zr (**Figures 6b-c-d**). This is a clear evidence of the interaction of Sr and Zr at the barrier layer, derived from a preliminary Zr diffusion during the barrier layer sintering process, as commented in the previous section. According to the STEM-EDX line scans for Ce, Sr and Zr across the grain boundary and Sr/Zr ratio (**Figures 6b-c**), the area 1 could be mainly composed of $SrZrO_3$. The results of High Resolution Transmission Electron Microscopy (HRTEM) and Nanobeam Beam Diffraction (NBD) images (**Figure 6d-e**) show that the analysed grain presented an inter-planar distance of 0.366 nm, which can be assigned to the (111) plane of the cubic $SrZrO_3$ structure with the Pm3m space group **[40]**.

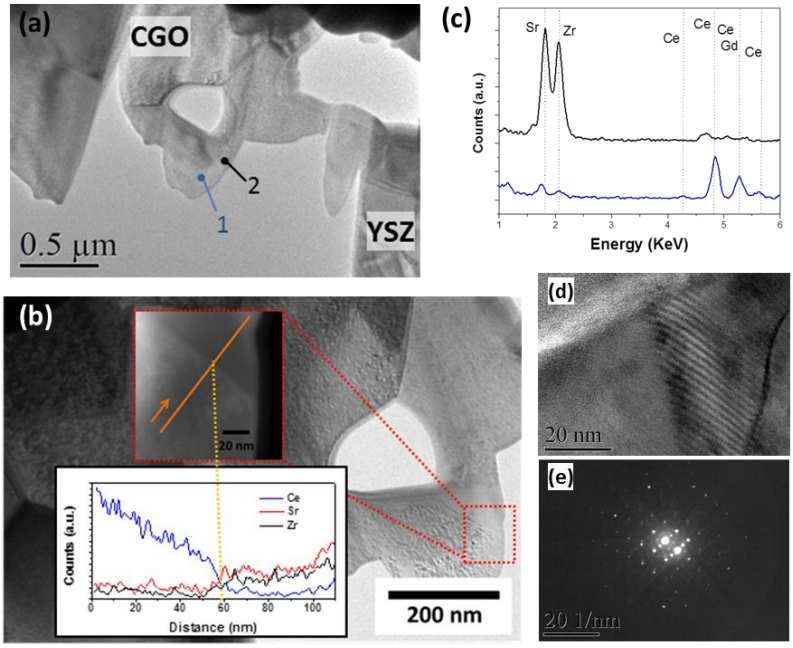

Figure 6. (a) and cross-sectional TEM and HAADF-STEM micrographs of CGO barrier layer, close to CGO/YSZ interface, of a TEM lamella extracted by FIB of the aged cell, **(b)** cross-sectional STEM-EDX line scans for Ce, Sr and Zr across a CGO/$SrZrO_3$ grain boundary, **(c)** two different areas (1 and 2) analysed by EDX,**(d)** High Resolution Transmission Electron Microscopy (HRTEM) image and **(e)** Nanobeam Beam Diffraction (NBD) of the area 1.

3.3 Role of CGO grain boundaries and free surfaces in the formation of $SrZrO_3$

In order to understand the role of grain boundaries and porosity on the diffusion of Sr and Zr and the consequent formation of $SrZrO_3$, TEM and STEM-EDX line scans were collected in different zones of CGO barrier layer (see **Figure 7**). As a general trend, Sr and Zr in the barrier layer are sharply concentrated at the pore surfaces, being its presence strongly reduced at the CGO bulk (**Figure 7 a-b**). On the other hand, as can be observed in **Figure 7 b-c**, grain boundaries also present a certain accumulation of these phases. Their relative concentration with respect to Ce is however clearly lower than in the case of free surfaces. It is also visible that Sr is more acutely limited to the grain boundary region, while Zr concentration smoothly decreases when penetrating in the grain bulk.

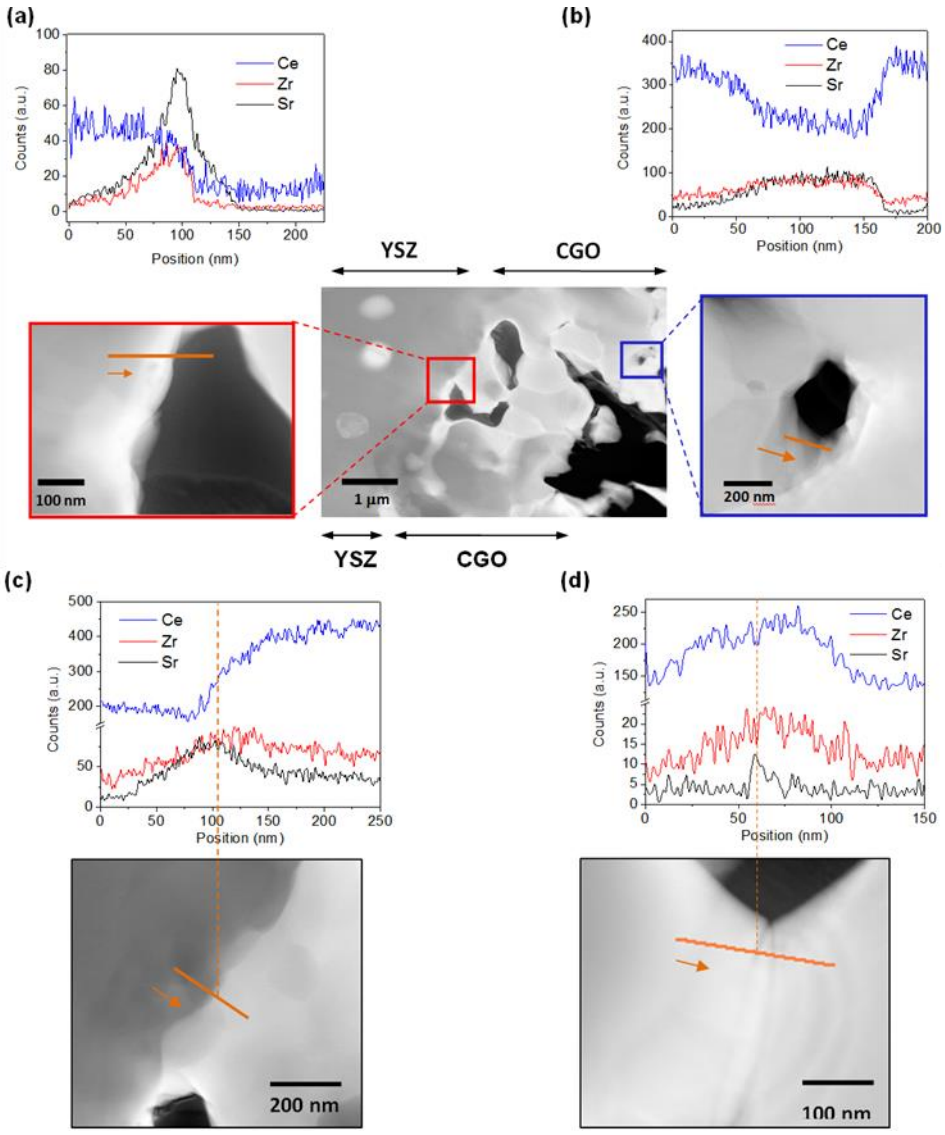

Figure 7. HAADF-STEM images and cross-sectional STEM-EDX line scans for Ce, Sr and Zr of: **(a)** CGO free surface close to the CGO/YSZ interface, **(b)** CGO free surface close to the LSCF/CGO interface, **(c)** and **(d)** CGO grain boundaries at the barrier layer, corresponding to the aged cell.

These results are consistent with some previous works dedicated to the study of Sr and Zr diffusion at CGO barrier layer in SOFCs. For instance, Wang et al. **[21]** observed that Sr and Zr were present all through a dense PLD CGO layer in a LSCF/10GDC/8YSZ system, and concluded that grain boundaries where acting as fast diffusion paths. Nevertheless, the amount of Zr and Sr was much higher in the surfaces of accidentally appearing cracks, which suggest that the diffusion along free surfaces is more pronounced. Another example is provided by Nurk et al **[28],** in which the diffusion through layers deposited by PLD, magnetron sputtering, spark plasma and screen printing is compared, using LSC as cathode material. Remarkably, for dense PLD deposited layers in which a pre-annealing at 1300ºC was conducted and the cathode was annealed at a lower temperature (950 ºC), Sr and Zr coexist at the LSCF/GDC interface. When higher temperature is

used for sintering the cathode (1100 ºC), this accumulation is also present at the GDC/YSZ interface, thus showing $SrZrO_3$ at both sides of CGO barrier layer. In contrast, for more porous layers, like the ones produced by screen printing, the Sr is mainly situated at the barrier layer-electrolyte interface **[9,28].** Apparently, Zr and Sr diffusion through the grain boundaries (i.e. main mechanism in dense layers) is of the same order at the corresponding annealing steps. In contrast, Sr diffusion through open surfaces during cathode annealing is much higher than the accumulated diffusion of Zr along the two successive sintering processes (i.e. barrier layer densification plus cathode sintering). The here studied CGO layers presents a relatively high porosity, which leads to a much more pronounced accumulation of Sr at the electrolyte-barrier layer zone that would explain the distribution of $SrZrO_3$ grains observed by complementary techniques: WDX, SIMS and STEM-EDX. The scheme in **Figure 8** summarizes this mechanism explaining the effect of the different steps of the cell manufacturing on the cation diffusion involved in the $SrZrO_3$ formation process. In a first stage, during the barrier layer sintering, a diffusion of Zr (and other elements like Ce, Gd, Y) into the CGO interlayer though grain boundaries and free surfaces occurs (**Figures 8a-b**). In a second stage, during the cathode sintering, preferential Sr diffusion takes place through free surfaces and, to a lesser extent, grain boundaries, leading to a $SrZrO_3$ formation at the Zr-rich grain boundaries and free surfaces (**Figure 8c**). In this way, $SrZrO_3$ is nucleated and grown near the CGO/YSZ interface, where both Sr and Zr are present in high concentrations and free surfaces are also available (**Figure 8d**).

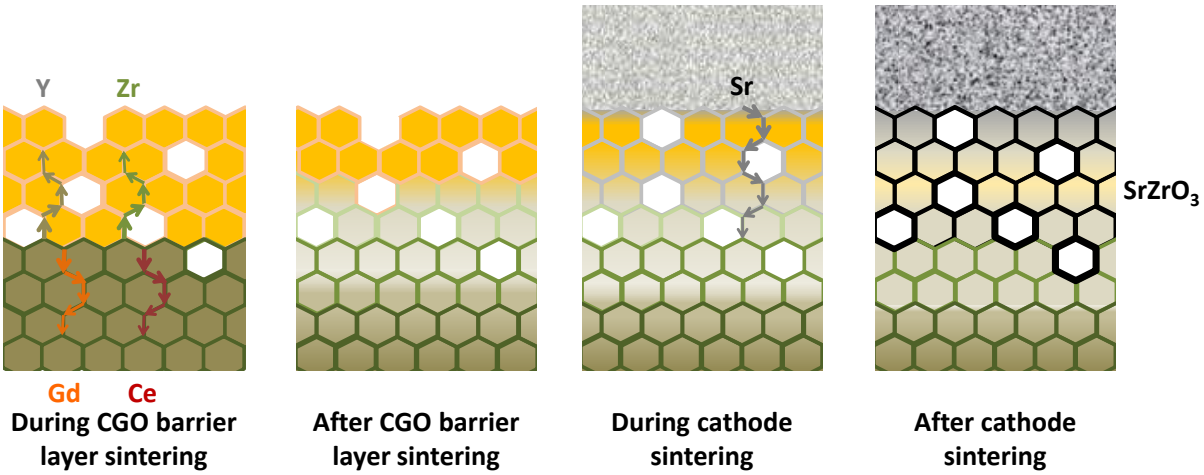

Figure 8. Sketch of the diffusion processes taking place during the different steps of the cell manufacturing, from sintering of CGO barrier layer to sintering of cathode, involved in the formation process of $SrZrO_3$.

4. Conclusions

A multi-scale study focused on the formation and degradation of a CGO diffusion barrier for solid oxide fuel cells was carried out in this work. A cell operated in a SOFC stack under real working conditions at 780ºC for 3000 h was compared with an identical pristine reference cell in order to determine the effects of ageing. Although strong cation inter-diffusion was observed at the CGO barrier layer region during the fabrication process, no significant differences were found between pristine and measured samples after operation. This fact demonstrates a potential improvement of the fabrication process and the initial performance of the cells while a good chemical stability of this type of barrier layers (once formed) during long-term operation.

Although the different analyses showed a significant inter-diffusion of Ce-Gd and Zr at CGO/YSZ interface, contrary to previous reports, no evidence of a $(Zr,Ce)O_2$-based solid solution formation in the barrier layer was found. Instead, the results indicate a composite-like coexistence of both phases. Remarkably, a gradual loss of Gd and its segregation to grain boundaries for migrating across the CGO barrier layer was revealed and identified as the major cause of the reduction of the layer conductivity at high sintering temperatures. New strategies to stop this mechanism should be defined to increase the initial performance of this type of solid oxide fuel cells.

The CGO free surfaces (grains facing pores) and, to a lesser extent, the grain boundaries (grains facing other grains) seem to be preferential pathways for both the Sr and Zr diffusion. An accumulation of Sr and Zr forming segregates of $SrZrO_3$ at the CGO/YSZ interface was observed. TEM observation revealed that the regions where CGO and YSZ are in close contact are free of the $SrZrO_3$. This could attenuate the impact of the formation of this insulating phase on the final performance ot the cell. The driving force of this $SrZrO_3$ grain formation may be associated to the high concentration of Zr near the electrolyte and the Sr diffusion through CGO grain boundaries and pores at the CGO barrier layer, which can act as sites nucleation and growth of $SrZrO_3$ grains.

All in all, it is possible to conclude that typically employed CGO diffusion barriers present cation inter-diffusion problems during the fabrication, while great chemical stability in operation. In order to increase the initial performance of SOFC containing CGO barrier layers further attention should be focused on the loss of gadolinium doping (and the corresponding decrease on ionic conductivity) as well as on the formation of insulating $SrZrO_3$, that, although isolated and out of the conduction pathways, could affect the functionality of different layers by altering their stoichiometry.

Acknowledgements

The research leading to these results have been obtained in the frame of the Endurance Project, funded by the European Union's Seventh Framework Programme (FP7/2007-2013) Fuel Cells and

Hydrogen Joint Undertaking (FCH-JU-2013-1) under grant agreement No 621207. The research was supported by the *Generalitat de Catalunya-AGAUR* (M2E exp. 2014 SGR 1638), and the European Regional Development Funds (ERDF, "FEDER Programa Competitivitat de Catalunya 2007-2013"). ICN2 acknowledges support from the Severo Ochoa Program (MINECO, Grant SEV-2013-0295).

References

[1] S. C. Singhal, K. Kendall, High Temperature Solid Oxide Fuel Cells: Fundamentals, Design and Applications, Elsevier, USA, 2003.

[2] J. Van Herle, D. Larrain, N. Autissier, Z. Wuillemin, M. Molinelli, D. Favrat. Modeling and experimental validation of solid oxide fuel cell materials and stacks. J. Eur. Ceram. Soc. 25 (2005) 2627-2632.

[3] K. Sasaki, K. Haga, T. Yoshizumi, D. Minen, C. Uryu, T. Oshima, T. Ogura, Y. Shiratori, K. Ito, M. Koyama, K. Yokomoto. Chemical durability of Solid Oxide Fuel Cells: Influence of impurities on long-term performance. J. Power Sources 196 (2011) 9130-9140.

[4] G. Ch. Kostogloudis, G. Tsiniarakis, Ch. Ftikos. Chemical reactivity of perovskite oxide SOFC cathodes and yttria stabilized zirconia. Solid State Ionics 135 (2000) 529-535.

[5] V. Miguel-Pérez, A. Martínez-Amesti, M. L. Nó, M. I. Arriortua. Compatibility between strontium-doped ferrite cathode and metallic interconnects in solid oxide fuel cells. J. Power Sources 280 (2015) 505-515.

[6] A. Tarancón, M. Burriel, J. Santiso, S. J. Skinner, J. A. Kilner. Advances in layered oxide cathodes for intermediate temperature solid oxide fuel cells. J. Mater. Chem. 20 (2010) 3799-3813.

[7] J. S. Hardy, J. W. Templeton, D. J. Edwards, Z. Lu, J. W. Stevenson. Lattice expansion of LSCF-6428 cathodes measured by in-situ XRD during SOFC operation. J. Power Sources, 198 (2012) 76-82.

[8] D. Montinaro, A. R. Contino, A. Dellai, M. Rolland. Determination of the impedance contributions in anode supported solid oxide fuel cells with (La,Sr)(Co,Fe)$O_{3-\delta}$ cathode. Int. J. Hydrogen Energy, 39 (2014) 21638-21646.

[9] S. Uhlenbruck, T. Moskalewicz, N. Jordan, H. J. Penkalla, H. P. Buchkremer. Element interdiffusion at electrolyte-cathode interfaces in ceramic high-temperature fuel cells. Solid Sate Ionics, 180 (2009) 418-423.

[10] F. Wang, M. E. Brito, K. Yamaji, D. H. Cho, M. Nishi, H. Kishimoto, T. Horita, H. Yokokawa. Effect of polarization on Sr and Zr diffusion behavior in LSCF/GDC/YSZ system. Solid State Ionics 262 (2014) 454-459.

[11] M. Kubicek, G. M. Rupp, S. Huber, A. Penn, A. K. Opitz, J. Bernardi, M. Stöger-Pollach, H. Hutter, J. Fleig. Surface chemistry of $La_{0.6}Sr_{0.4}CoO_{3-\delta}$ thin films and its impact on the oxygen surface exchange resistance. Phys. Chem. Chem. Phys. 16 (2014) 2715-2726.

[12] D. The, S. Grieshammer, M. Schroeder, M. Martin, M. Al. Daroukh, F. Tietz, J. Schefold, A. Brisse. Microstructural comparison of solid oxide electrolyser cells operated for 6100 h and 9000 h. J. Power Sources 275 (2015) 901-911.

[13] K. Eguchi, T. Setoguchi, T. Inoue, H. Arai. Electrical properties of ceria-based oxides and their application to solid oxide fuel cells Solid State Ionics 52 (1992) 165-172.

[14] T. Klemensø, J. Nielsen, P. Blennow, A. H. Persson, T. Stegk, B. H. Christensen, S. Sønderby. High performance metal-supported solid oxide fuel cells with Gd-doped ceria barrier layers. J. Power Sources 196 (22) (2011) 9459-9466.

[15] P. Plonczak, M. Joost, J. Hjelm, M. Søgaard, M. Lundberg, P. V. Hendriksen A high performance ceria based interdiffusion barrier layer prepared by spin-coating. J. Power Sources 196 (2011) 1156-1162.

[16] F. P. F. van Berkel, Y. Zhang-Steenwinkel, G. P. J. Schoemakers, M. M. A. van Tuel, G. Rietveld. Document Enhanced ASC performance at 600°C by ceria barrier layer optimization. ECS Transactions 25 (2) (2009) 2717-2726.

[17] M. Morales, J. J. Roa, X. G. Capdevila, M. Segarra, S. Pinol. Effect of sintering temperature on the mechanical properties of film $Gd_{0.2}Ce_{0.8}O_{1.9}$ electrolyte for SOFCs using nanoindentation. J. New Mater. Elechem. Syst. 12 (2009) 187-193.

[18] P. Plonczak, M. Joost, J. Hjelm, M. Søgaarda, M. Lundberg, P. V. Hendriksen. A high performance ceria based interdiffusion barrier layer prepared by spin-coating. J. Power Sources 196 (2011) 1156-1162.

[19] A. Martínez-Amesti, A. Larrañaga, L. M. Rodríguez-Martínez, M. L. Nó, J. L. Pizarro, A. Laresgoiti, M. I. Arriortua. Reactivity between La(Sr)FeO_3 cathode, doped CeO_2 interlayer and yttria-stabilized zirconia electrolyte for solid oxide fuel cell applications. J. Power Sources 192 (2008) 151-157.

[20] A. Martínez-Amesti, A. Larrañaga, L. M. Rodríguez-Martínez, M. L. Nó, J. L. Pizarro, A. Laresgoiti, M. I. Arriortua. Chemical compatibility between YSZ and SDC sintered at different atmospheres for SOFC applications. J. Power Sources, 192 (2009) 151-157.

[21] F. Wang, M. Nihi, M. E. Brito, H. Kishimoto, K. Yamaji, H. Yokokawa, T. Horita. Sr and Zr diffusion in LSCF/10GDC/8YSZ triplets for solid oxide fuel cells (SOFCs). J. Power Sources, 258 (2014) 281-289.

[22] Hi. Mitsuyasu, Y. Nonaka, K. Eguchi. Analysis of solid state reaction at the interface of yttria-doped ceria/yttria-stabilized zirconia. Solid State Ionics 113-115 (1998) 279-284.

[23] C. V. Raman, K. S. Krishnan. A New Type of Secondary Radiation. Nature 121 (1928) 501-502.

[24] W. H. Weber, R. Merlin. Raman Scattering in Materials Science, New York: Springer-Heidelberg, 2000.

[25] M. A. Banares. In Situ Spectroscopy of Catalysts, USA: American Scientific Publishers, 2004.

[26] Smith, E. & Dent, G., Modern Raman Spectroscopy: A Practical Approach, Hoboken, NJ: Wiley, 2005.

[27] D. E. Pfoertsch, G. I. McCarthy, Penn State University, University Park, Pennsylvania, USA, ICDD Grant-in-Aid (1977).

[28] G. Nurk, M. Vestli, P. Möller, R. Jaaniso, M. Kodu, H. Mändar, T. Romann, R. Kanarbik, E. Lusta. Mobility of Sr in Gadolinia Doped Ceria Barrier Layers Prepared Using Spray Pyrolysis, Pulsed Laser Deposition and Magnetron Sputtering Methods. Journal of The Electrochemical Society, 163 (2016) F88-F96.

[29] A. Tsoga, A. Gupta, A. Naoumidis, P. Nikolopoulos. Gadolinia-doped ceria and yttria stabilized zirconia interfaces: Regarding their application for SOFC technology. Acta Mater. 48 (2000) 4709-4714.

[30] R. Knibbe, J. Hjelm, M. Menon, N. Pryds, M. Sogaard, H. J. Wang, K. Neufeld. Cathode-electrolyte interfaces with CGO barrier layers in SOFC. J. Am. Ceram. Soc., 93(9) (2010) 2877-2883.

[31] A. Martínez-Amesti, A. Larrañaga, L. M. Rodríguez-Martínez, A. T. Aguayo, J. L. Pizarro, M. L. Nó, A. Laresgoiti, M. I. Arriortua. Reactivity between La(Sr)FeO_3 cathode, doped CeO_2 interlayer and yttria-stabilized zirconia electrolyte for solid oxide fuel cell applications. J. Power Sources, 185 (2008) 401-410.

[32] M. Price, J. Dong, X. Gu. Formation of YSZ–SDC Solid Solution in a Nanocrystalline Heterophase System and Its Effect on the Electrical Conductivity. J. Am. Ceram. Soc., 88 (7) (2005) 1812-1818.

[33] G. A. Tompsett, N. M. Sammes, O. Yamamoto. Ceria-Yttria-Stabilized Zirconia Composite Ceramic Systems for Applications as Low-Temperature Electrolytes. J. Am. Ceram. Soc., 80 (1997) 3181-3186.

[34] Y. Hemberger, N. Wichtner, C. Berthold, K. G. Nickel. Quantification of Yttria in Stabilized Zirconia by Raman Spectroscopy. Int. J. Appl. Ceram. Technol. 13 (2016) 116–124.

[35] M. Kuhn, S.R. Bishop, J.L.M. Rupp, H.L. Tuller. Structural characterization and oxygen nonstoichiometry of ceria-zirconia ($Ce_{1-x}Zr_xO_{2-\delta}$) solid solutions. Acta Mater. 61 (2013) 4277-4288.

[36] J.R. McBride, K.C. Hass, B.D. Poindexter, W.H. Weber. Raman and x-ray studies of $Ce_{1-x}RE_xO_{2-y}$, where RE=La, Pr, Nd, Eu, Gd, and Tb. J. Appl. Phys. 76 (4) (1994) 2435-244.

[37] N. Yang, Y. Shi, S. Schweiger, E. Strelcov, A. Belianinov, V. Foglietti, P. Orgiani, G. Balestrino, S. V. Kalinin, J. L. M. Rupp, C. Aruta. Role of Associated Defects in Oxygen Ion Conduction and Surface Exchange Reaction for Epitaxial Samaria-Doped Ceria Thin Films as Catalytic Coatings. Appl. Mater. Interfaces 8 (2016) 14613-14621.

[38] B.C.H. Steele. Appraisal of $Ce_{1-y}Gd_yO_{2-y/2}$ electrolytes for IT-SOFC operation at 500ºC. Solid State Ionics 129 (2000) 95-110.

[39] M. Izuki, M. E. Brito, K. Yamaji, H. Kishimoto, D-H. Cho, T. Shimonosono, T. Horita, H. Yokokawa. Interfacial stability and cation diffusion across the LSCF/GDC interface. J. Power Sources, 196 (2011) 7232-7236.

[40] R. I. Eglitis. Ab Initio Calculations of the Atomic and Electronic Structure of $SrZrO_3$ (111) Surfaces. Ferroelectrics, 436 (2012) 5-11.